Journal of Alloys and Compounds 509 (2011) 2450–2460

Contents lists available at ScienceDirect

Journal of Alloys and Compounds

journal homepage: www.elsevier.com/locate/jallcom

High temperature friction and wear behaviour of sputter-deposited nanocrystalline $(Mo_xCr_{1-x})_5Si_3$ films by a double cathode glow discharge technique

Jiang Xu*, Linlin Liu, Xiaolin Lu

Department of Material Science and Engineering, Nanjing University of Aeronautics and Astronautics, 29 Yudao Street, Nanjing 210016, Jiangsu, PR China

ARTICLE INFO

Article history:
Received 22 September 2010
Received in revised form 3 November 2010
Accepted 5 November 2010
Available online 12 November 2010

Keywords:
Friction and wear
Nanocrystalline films
Refractory materials
Surface modification

ABSTRACT

In order to improve the wear resistance of titanium alloys, five kinds of sputter-deposited nanocrystalline $(Mo_xCr_{1-x})_5Si_3$ (x = 1, 0.78, 0.75, 0.64, 0.57) films with average grain size 8 nm were fabricated on a substrate of Ti6Al4V alloy by means of a double cathode glow discharge technique. The microstructure and composition of the as-deposited films were characterized by scanning electron microscope (SEM), transmission electron microscopy (TEM), X-ray diffraction (XRD) and energy dispersive spectrometer (EDS). Nanoindentation was used to measure hardness (H) and elastic modulus (E) of the as-deposited films. High temperature friction and wear properties of the as-deposited films were investigated against ZrO_2 ceramic balls by a ball-on-disk system at 600 °C. Compared with the Ti6Al4V alloy, the friction coefficient values of the nanocrystalline $(Mo_xCr_{1-x})_5Si_3$ films were reduced by 0.2–0.3, and specific wear rates decreased by two orders of magnitude and were around or lower than 10^{-6} mm^3/(N m) at the load ranging from 3.3 N to 4.8 N. The friction coefficient and specific wear rates of the as-deposited films relied on the Cr content in the nanocrystalline $(Mo_xCr_{1-x})_5Si_3$ films, and the higher the Cr content, the lower friction coefficient and wear rates.

1. Introduction

Titanium alloys, due to their excellent combination of high specific strength, low density, outstanding corrosion resistance and good biocompatibility, are a good choice to be used for structural applications in the aerospace, automotive, chemical, marine and biomedical industries [1,2]. However, the poor tribological performance of titanium alloys, manifested by high friction coefficients and severe adhesive wear with a strong tendency to seizing and low abrasion resistance, extensively limits their practical applications where wear resistance is required [3,4]. Particularly, under dry sliding at high temperature conditions, the degradation is even worse because the passive oxide layer is easily removed by spalling or microfragmentation, and subsequent reoxidation of the exposed metal surface occurs [5]. The poor tribological properties can be attributed to the inherent nature of titanium alloys, including electron configuration, crystal structure and lubrication characteristics [6]. Therefore, a number of different surface modification techniques, such as laser surface treatment plasma [7], immersion ion implantation (PIII) [8], chemical vapor deposition (CVD) [9,10], and physical vapor deposition (PVD) [11,12], were recently applied to improve the tribological behaviour of titanium alloys.

In recent years, refractory transition metal silicides alloys have attracted much attention as promising high temperature structural materials because of their outstanding balance of high melting point, high strength, low density, high elastic modulus and excellent creep and oxidation resistance [13–15]. Compared with other refractory metals, the silicides of molybdenum have generally exhibited good oxidation, corrosion resistance and a lower density [16]. In the Mo–Si system, there are three compounds, i.e. $C11_b$-structured $MoSi_2$, $D8_m$-structured Mo_5Si_3, and A15-structured Mo_3Si. Among the compounds of molybdenum silicides, $D8_m$-structured Mo_5Si_3 is the most refractory compound having a melting point of 2180 °C, thus having a great potential for structural applications in harsh environments. Mo_5Si_3 shows the very high hardness up to temperatures of 1200 °C and has been regarded as a self-lubricating phase, due to the fact that Mo_5Si_3 reacts with the oxygen at the contact surface and forms self-lubricating MoO_3 under unlubricated sliding wear conditions [17]. Thus, Mo_5Si_3 is expected to be a new class of wear resistant candidate materials for those moving mechanical components working under high-temperature aggressive tribological conditions. A number of papers have addressed the mechanical properties and oxidation behaviour of Mo_5Si_3 [18–20]. However, as far as the authors know, no literature has been reported with regard to the wear resistance of Mo_5Si_3

* Corresponding author. Tel.: +86 02552112626.
E-mail address: xujiang73@nuaa.edu.cn (J. Xu).

0925-8388/$ – see front matter © 2010 Elsevier B.V. All rights reserved.
doi:10.1016/j.jallcom.2010.11.051

metal silicide alloys either as bulk or coating materials, much less the nanocrystalline Mo_5Si_3.

In our previous work [21,22], we have found that the double-cathode glow discharge technique can be used to synthesize nanocrystalline Al_2Mg film and nanocrystalline Cr_3Si film with a grain size of <5 nm on magnesium alloy and titanium alloy, respectively. The purpose of this investigation is to overcome the poor tribological performance of Ti6Al4V alloy. Five kinds of nanocrystalline $(Mo_xCr_{1-x})_5Si_3$(x = 1, 0.78, 0.75, 0.64, 0.57) films have been prepared on Ti6Al4V alloy substrates by double cathode glow discharge. The influences of chromium content on the high temperature friction and wear properties of $(Mo_xCr_{1-x})_5Si_3$(x = 1, 0.78, 0.75, 0.64, 0.57) films against ZrO_2 ceramic balls have been investigated by a ball-on-disk type tribotester. In an effort to understand the mechanisms controlling the wear processes and tribological behaviours, the morphologies of the worn surfaces and isothermal oxidation behaviour of the films were studied.

2. Experimental method

The nanocrystalline $(Mo_xCr_{1-x})_5Si_3$ films were deposited onto Ti6Al4V alloy substrates by a double cathode glow discharge apparatus which was described in our previous papers [21]. In the process of double-cathode glow discharge, one cathode is fabricated as source (target) by desired sputtering materials, and the other cathode is as substrate materials. When two different voltages are applied to the two cathodes, glow discharge comes into being. The glow discharge sputtering conditions are: base pressure, 4×10^{-4} Pa; target electrode bias voltage, −900 V; substrate bias voltage, −350 V; substrate temperature, 800 °C; working pressure, 35 Pa; and parallel distance between the source electrode and the substrate, 15 mm and treatment time of 3 h. The sputter targets were fabricated by employing cold compacting technology under a pressure of 600 MPa from ball-milled Mo (99.99% purity), Cr (99.99% purity) and Si powders (99.99% purity). The substrate was Ti6Al4V alloy disks of 40 mm in diameter and 3 mm in thickness. The substrates were mechanically ground and progressively polished with a diamond paste. The polished substrates were then washed in acetone and ethanol by an ultrasonic washer. Five kinds of $(Mo_xCr_{1-x})_5Si_3$ (x = 1, 0.78, 0.75, 0.64, 0.57) films were deposited onto substrate material by the double cathode glow discharge using five targets with different stoichiometric ratios ($Mo_{50}Si_{50}$, $Mo_{40}Cr_{10}Si_{50}$, $Mo_{35}Cr_{15}Si_{50}$, $Mo_{30}Cr_{20}Si_{50}$ and $Mo_{25}Cr_{25}Si_{50}$), respectively.

Phase composition of the as-deposited films was characterized with X-ray diffractometry (XRD, D8ADVANCE) operated at 35 kV and 40 mA. X-ray data were collected using a 0.1° step scan with a count time of 1 s. The etching of the $(Mo_xCr_{1-x})_5Si_3$ films was accomplished with the use of Kroll's reagent (10 ml HNO_3, 4 ml HF and 86 ml distilled water) for 20–30 s. The cross-sectional morphology and chemical composition of the as-deposited films were studied by scanning electron microscopy (SEM, Quanta200, FEI Company) and energy-dispersive X-ray spectroscopy (EDX). Transmission electron microscopy (TEM) and high-resolution transmission electron microscopy (HRTEM) images were observed by JEOL JEM-2010 at an accelerating voltage of 200 kV. Thin foils samples for TEM observation were cut from as-deposited film and were prepared by single jet electropolishing from the untreated side of the substrate.

The nanohardness and the Young's modulus of as-deposited film were obtained by the nanoindentation tester (NHT) equipped with a Berkovich tip. This system, developed by CSEM Instruments, comprises two distinct components: a measuring head for performing nanoindentations and an optical microscope for selecting a specific sample site prior to indentation, and for checking the location of the imprint after indentation. The system has the load and displacement resolutions of 10 mN and 1 nm, respectively. Fused silica was used as a standard sample for the initial tip calibration. The indentation was worked by driving the indenter at a constant loading rate of 40 mN/min into the materials with the maximum applied load of 20 mN. The standard analysis procedure proposed by Oliver and Pharr [23] was used to determine the hardness of the specimens from the unloading curve. For each indentation displacement, nanoindentation tests were conducted at five different locations to ensure repeatability of the experimental data.

Friction and wear tests were performed on a HT-500 tribometer with ball-on-disk configuration under dry sliding conditions at 600 °C. The as-deposited films specimens were tested against a 3 mm diameter ZrO_2 ceramic ball counterpart (nominal hardness HV = 13 GPa). The tests were carried out at normal load of 3.3 N, 3.8 N, 4.3 N and 4.8 N, and the sliding speed of the counterpart ball was 22 cm/s. The total sliding distance for the test was 633 m. The friction coefficient is monitored on-line during the tests. The worn volume loss was assessed by calculating the cross-sectional areas of wear tracks developed on the surface of the samples, after measuring their width and depth by a MicroXAM™ non-contact optical profilometer (ADE Phase-Shift, USA). The morphology, chemical compositions and phase identification of worn surfaces and wear debris were analyzed by SEM-EDX and XRD.

3. Results

3.1. Microstructures and phase analysis

The X-ray diffraction patterns of the five kinds of as-deposited $(Mo_xCr_{1-x})_5Si_3$(x = 1, 0.78, 0.75, 0.64, 0.57) films are presented in Fig. 1. The diffraction patterns are characterized by a set of broad peak indexed as $D8_m$-structured Mo_5Si_3 phase (JCPDS Card No.76-1578), indicating that all the as-deposited films consist of a single phase of $(Mo_xCr_{1-x})_5Si_3$, and phase composition of the films is independent of the substitution of Cr for Mo. This is due to the fact that Cr_5Si_3–Mo_5Si_3 is an infinitive solid-solute system and the chemical bond of Cr atom in $D8_m$ system is considered to be similar to that of Mo atoms. Thereby, the formation of second phases never occurs with the substitution of Cr for Mo site in Mo_5Si_3. Furthermore, it is evident that shift of the diffraction peaks strongly depends on the Cr content in the films. Owing to the atomic radius of Cr element is smaller than that of Mo element, the diffraction peaks gradually shift in the direction of larger angles in comparison to the powder diffraction file (PDF) data for Mo_5Si_3 with the increasing addition of Cr to Mo_5Si_3, indicating a lattice contraction. This is in accordance with the results reported in reference [24].

Fig. 2 shows SEM cross-sectional morphologies and EDS line profiles of as-deposited Mo_5Si_3 film and $(Mo_{0.75}Cr_{0.25})_5Si_3$ film formed on Ti6Al4V alloy. Clearly, the two films are continuous and compact, and combined well with the Ti6Al4V alloy substrate without pores and micro-cracks. The microstructure of two kinds of $(Mo_xCr_{1-x})_5Si_3$(x = 1, 0.75) films can be classified into two uniform layers, namely, deposited layer and diffusion layer. The deposited layer contains mostly Mo (or Mo + Cr) and Si, and the Mo (or Mo + Cr) and Si concentrations across the depth of deposited layer remain almost constant with a molar ratio of Mo (or Mo + Cr) to Si close to 1.66, indicating that the deposited layer is composed of single $(Mo,Cr)_5Si_3$ phase. In order to understand the constituent phases of the diffusion layer, the phases present in the diffusion layer are identified by X-ray diffraction after removing a part of Mo_5Si_3 deposited layer, and its XRD pattern is plotted in Fig. 1 (curve 2). A comparison between the curve 1 and curve 2 (Fig. 1) shows that the diffusion layer is a composite of β-Ti, α″ and α′ phases. Because the dominant diffusion element in Mo_5Si_3 phase is Mo [25], Mo element diffuses inwards into interface between the deposited layer and substrate, leading to the phase transformation of $\beta \rightarrow \alpha'' \rightarrow \alpha'$, which occurs from outside to inside for the different Mo contents in the diffusion layer [26]. Combining the XRD results and EDS anal-

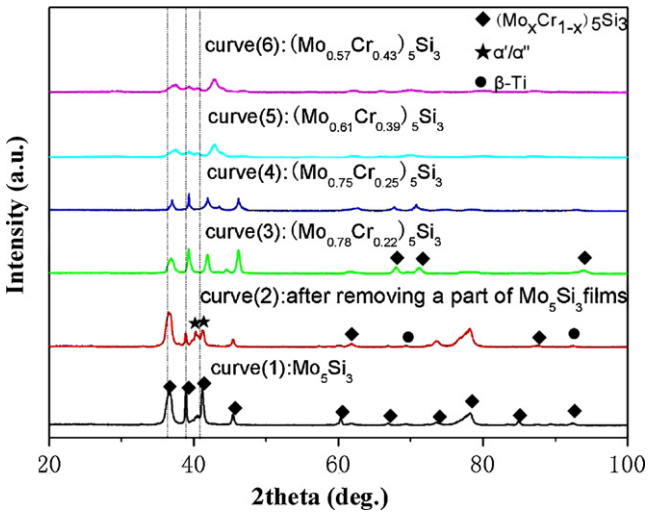

Fig. 1. XRD pattern of the sputter-deposited $(Mo_xCr_{1-x})_5Si_3$ films.

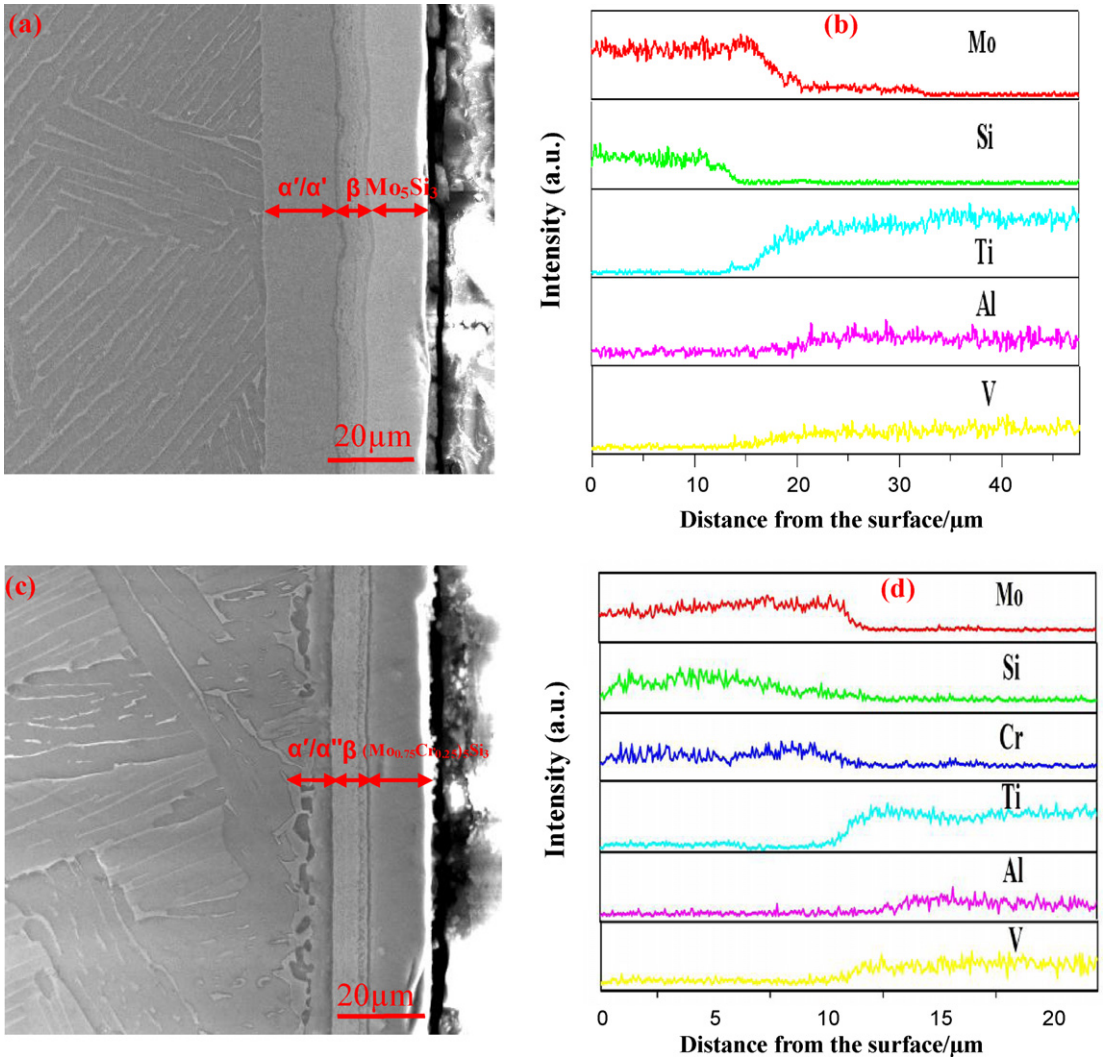

Fig. 2. SEM cross-section image and element line scanning EDS analyses of the sputter-deposited $(Mo_xCr_{1-x})_5Si_3$ films formed on Ti6Al4V alloy: (a and b) Mo_5Si_3 film; (c and d) $(Mo_{0.75}Cr_{0.25})_5Si_3$ film.

ysis, conclusions can be made that according to the different Mo contents, Mo diffusion layer may be subdivided into β phase layer with high Mo content (>10 wt.%) and α″/α′ layer with low Mo content (<10 wt.%), as shown in Fig. 2. Beyond this, it is worthwhile to note that the thickness of diffusion layer is affected by its Cr content and the higher Cr content results in the thinner thickness of diffusion layer, implying that Cr element restricts Mo element migrating from the deposited layer to substrate. The gradient distribution of alloying elements in the diffusion layer offers a smooth transition of mechanical properties, which is suitable to improve the adhesion strength of the films on the Ti6Al4V substrate and to relieve stress concentration between the films and substrate when the films are subjected to external stress.

Fig. 3 shows the typical HRTEM image and selected area diffraction (SAED) patterns of Mo_5Si_3 film. It is clear that the microstructure of Mo_5Si_3 film is characterized by ultrafine spherical grains with random crystallographic orientations, and the average grain size is about 8 nm according to a statistical grain size distribution of a number of TEM images. The space of the lattice fringes of nanocrystalline with the marks of A can be calculated as 0.211 nm, corresponding to the interspacing of the (4 1 1) planes of $D8_m$-structured Mo_5Si_3. The first five diffraction rings of SAED (inset in Fig. 3) represent (2 2 0), (3 1 0), (4 1 1), (4 3 1) and (5 2 1) planes of $D8_m$ crystal structure Mo_5Si_3, respectively.

3.2. Nanoindentation test

Fig. 4a shows the representative load–displacement (P–h) curves of the five kinds of nanocrystalline $(Mo_xCr_{1-x})_5Si_3$(x = 1,

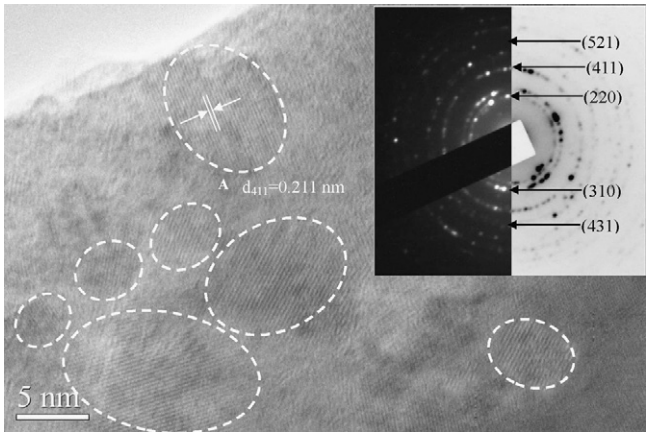

Fig. 3. HRTEM images and the corresponding SAED pattern of the nanocrystalline Mo_5Si_3 film. Some of the nanocrystallites are circled for easier recognition. The space of the lattice fringes of nanocrystalline marked A can be calculated as 0.211 nm, which correspond to the interspacing of the (4 1 1) plane of $D8_m$-structured Mo_5Si_3.

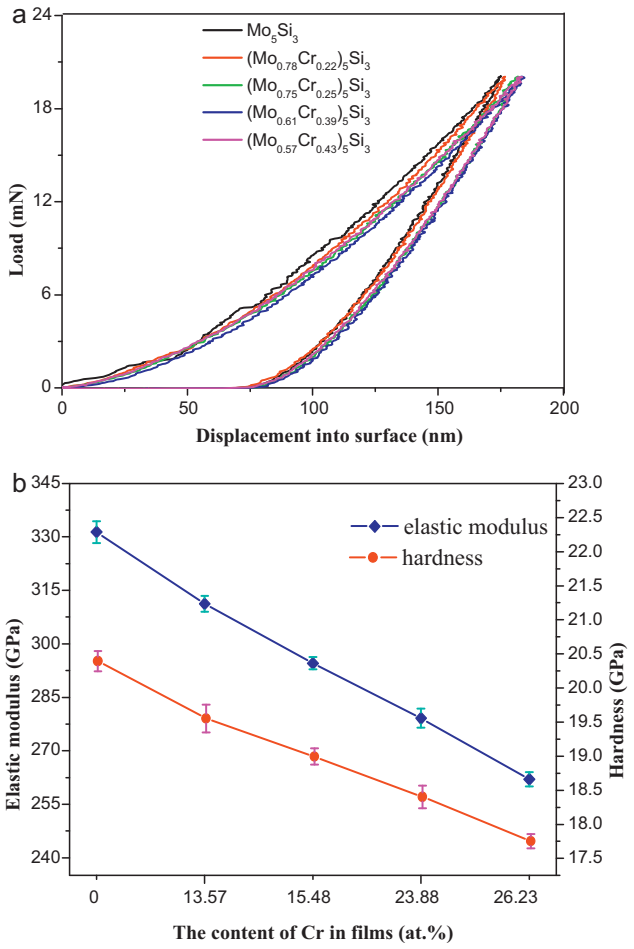

Fig. 4. (a) Load–displacement curves of the nanocrystalline $(Mo_xCr_{1-x})_5Si_3$ (x = 1, 0.78, 0.75, 0.61, 0.57) films and (b) hardness and elastic modulus of nanocrystalline $(Mo_xCr_{1-x})_5Si_3$ films.

0.78, 0.75, 0.64, 0.57) films under a maximum load of 20 mN. It must be additionally ensured that the indentation depth is notably lower than 10% of the films thickness in order that the contribution to mechanical properties from its substrate is negligible. In Fig. 4b the variation of hardness and elastic modulus with the Cr content in the films is plotted. The hardness and elastic modulus of $(Mo_xCr_{1-x})_5Si_3$(x = 1, 0.78, 0.75, 0.64, 0.57) films decrease with the increasing addition of Cr. It is worth mentioning here that the nanocrystalline $(Mo_xCr_{1-x})_5Si_3$(x = 1, 0.78, 0.75, 0.64, 0.57) films show higher values of hardness and elastic modulus than coarse grain of Mo_5Si_3 reported in the literature (H = 11.48 GPa, E = 260 GPa) [27]. The similar findings were also observed in our previous work [22].

3.3. Sliding friction and wear behaviours of nanocrystalline $(Mo_xCr_{1-x})_5Si_3$ film

Fig. 5 shows the variation in friction coefficient and specific wear rate as function of normal load for Ti6Al4V alloy sliding against ZrO_2 ceramic balls at 600 °C. The mean values of friction coefficient are determined from the steady-state stage excluding initial rising in the running period. With an increase in the applied normal load from 3.3 to 4.8 N, Ti6Al4V alloy exhibits an increasing trend in the mean friction coefficient and specific wear rate. The increase of the friction coefficient with the increase of the applied normal load is probably due to the growth of actual contact area on both the slide surfaces, the generation of the wear debris as well

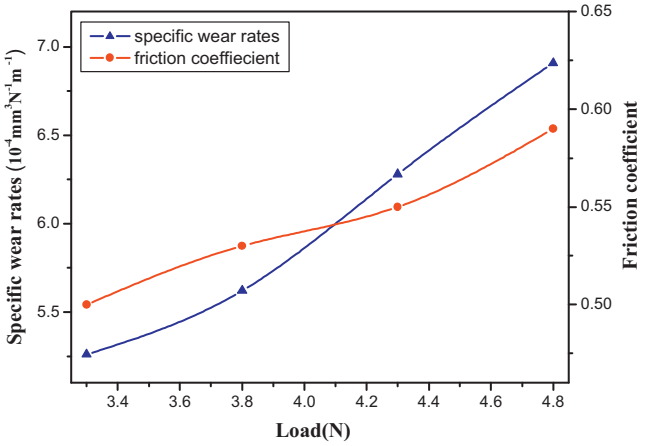

Fig. 5. The variation of friction coefficient and specific wear rate with the normal load for Ti6Al4V alloy under dry sliding conditions at 600 °C.

as surface softening arising from the friction thermal effect under dry friction condition. The specific wear rate is in the order of 5 to7 $\times 10^{-4}$ mm^3/(N m) when the applied normal load is in the range of 3.3–4.8 N. The mean friction coefficients of five kinds of nanocrystalline $(Mo_xCr_{1-x})_5Si_3$ films are plotted as a function of Cr content in the films and the applied normal load under wear test temperature of 600 °C, as shown in Fig. 6. The mean friction coefficients increase with increasing the applied load for all the as-deposited films and decrease with increasing Cr content in the films at the same applied load. In the investigated range of loads, the mean friction coefficients of the nanocrystalline $(Mo_xCr_{1-x})_5Si_3$ films are reduced by 0.2–0.3 as compared to the uncoated substrate. Fig. 7 shows the specific wear rates of the nanocrystalline $(Mo_xCr_{1-x})_5Si_3$ films sliding against ZrO_2 ceramic balls at different normal loads under dry sliding conditions at 600 °C. It can be seen that the specific wear rates of nanocrystalline $(Mo_xCr_{1-x})_5Si_3$ films are around or slightly lower than 10^{-6} mm^3/(N m) at different normal loads, which are two orders of magnitude less than that of Ti6Al4V alloy. Moreover, the specific wear rates decrease with increasing Cr content in the films at the same applied load.

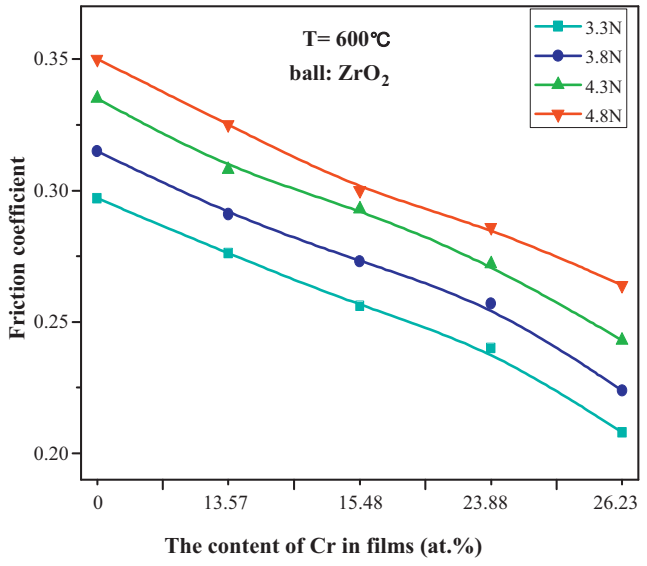

Fig. 6. Variation of friction coefficient as function of Cr content in the films and the applied normal load for nanocrystalline $(Mo_xCr_{1-x})_5Si_3$ films sliding against ZrO_2 ceramic balls at 600 °C.

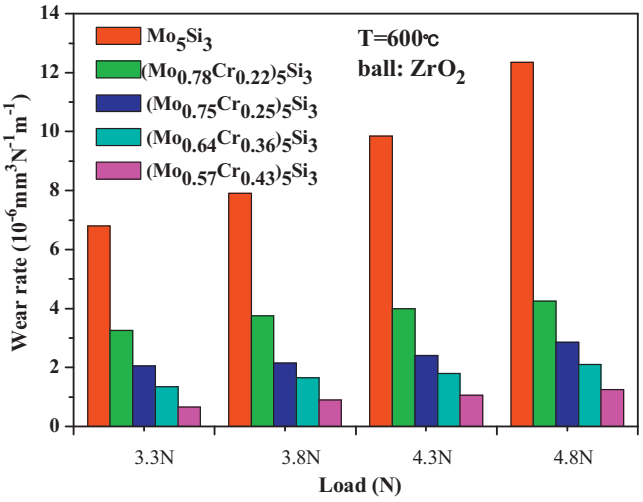

Fig. 7. The specific wear rate of the nanocrystalline $(Mo_xCr_{1-x})_5Si_3$ films against ZrO_2 ceramic balls at different normal loads under dry sliding conditions at 600 °C.

SEM micrographs of the worn surfaces of Ti6Al4V alloy at the applied normal loads of 3.8 N and 4.8 N under test temperature of 600 °C, are shown in Fig. 8. Typically, the worn surfaces exhibit deep grooves, delamination and severe plastic deformation. Results of EDS analysis show that the wear tracks have higher oxygen content than the surrounding unworn surfaces, suggesting that the oxide layer is produced by the reaction of worn surfaces with the oxygen at the contact surface. Sliding wear under dry sliding condition, especially at elevated temperature, large amount of frictional heat produced together with the environment temperature would not only cause thermal softening of Ti6Al4V alloy but also accelerate the formation of oxide scale on its surface. Owing to a high temperature at the contact surface, the hardness of Ti6Al4V alloy decreases significantly and is too low to support the relatively hard oxide layer, making the oxide scale flaked off easily [28]. Subsequently, the detached hard oxides entrapped between the contra-wear surfaces accelerate the damage of worn surface, leading to the wear mechanism transformation from two-body to three-body abrasive wear. Besides, the higher normal load results in friction contact temperature, the degradation is even worse, characterized by a wider wear track and deeper plowing grooves. Chemical composition analysis and morphological observation of wear debris give further insight into wear mechanism involved. The wear debris consists of irregular large flakes and a little fine powder (see Fig. 9a), and is highly

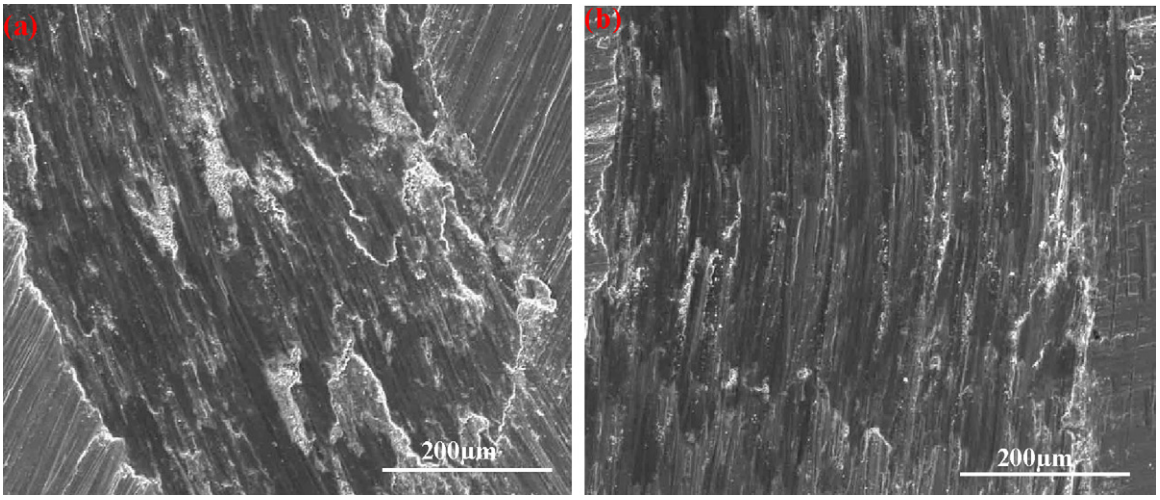

Fig. 8. Worn surface morphologies of Ti6Al4V alloy at normal loads of 3.8 N (a) and 4.8 N (b) under dry sliding conditions at 600 °C.

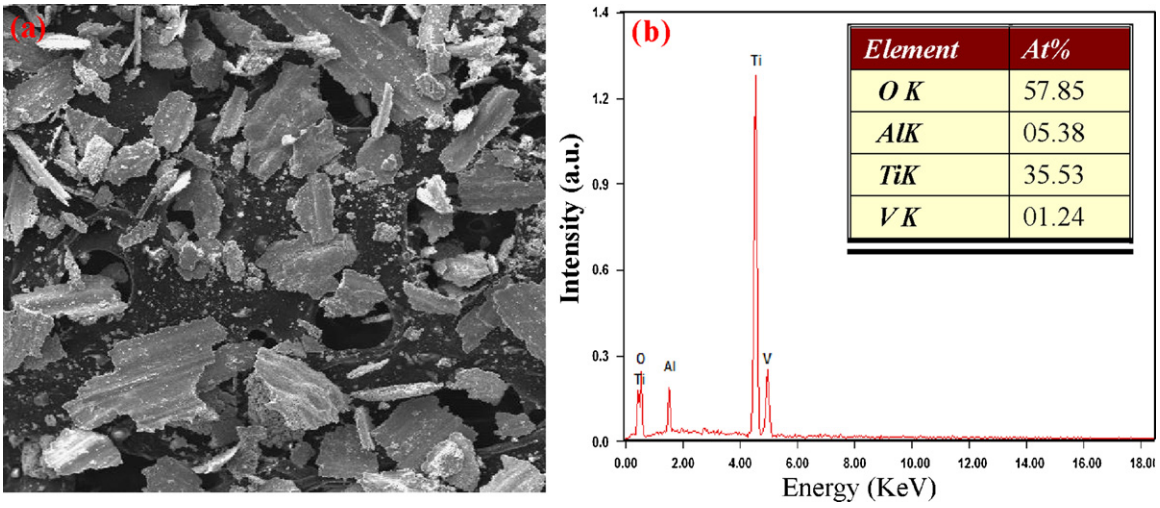

Fig. 9. Wear debris from Ti6Al4V/ZrO_2 ball sliding pairs: (a) wear debris morphology and (b) EDS analysis.

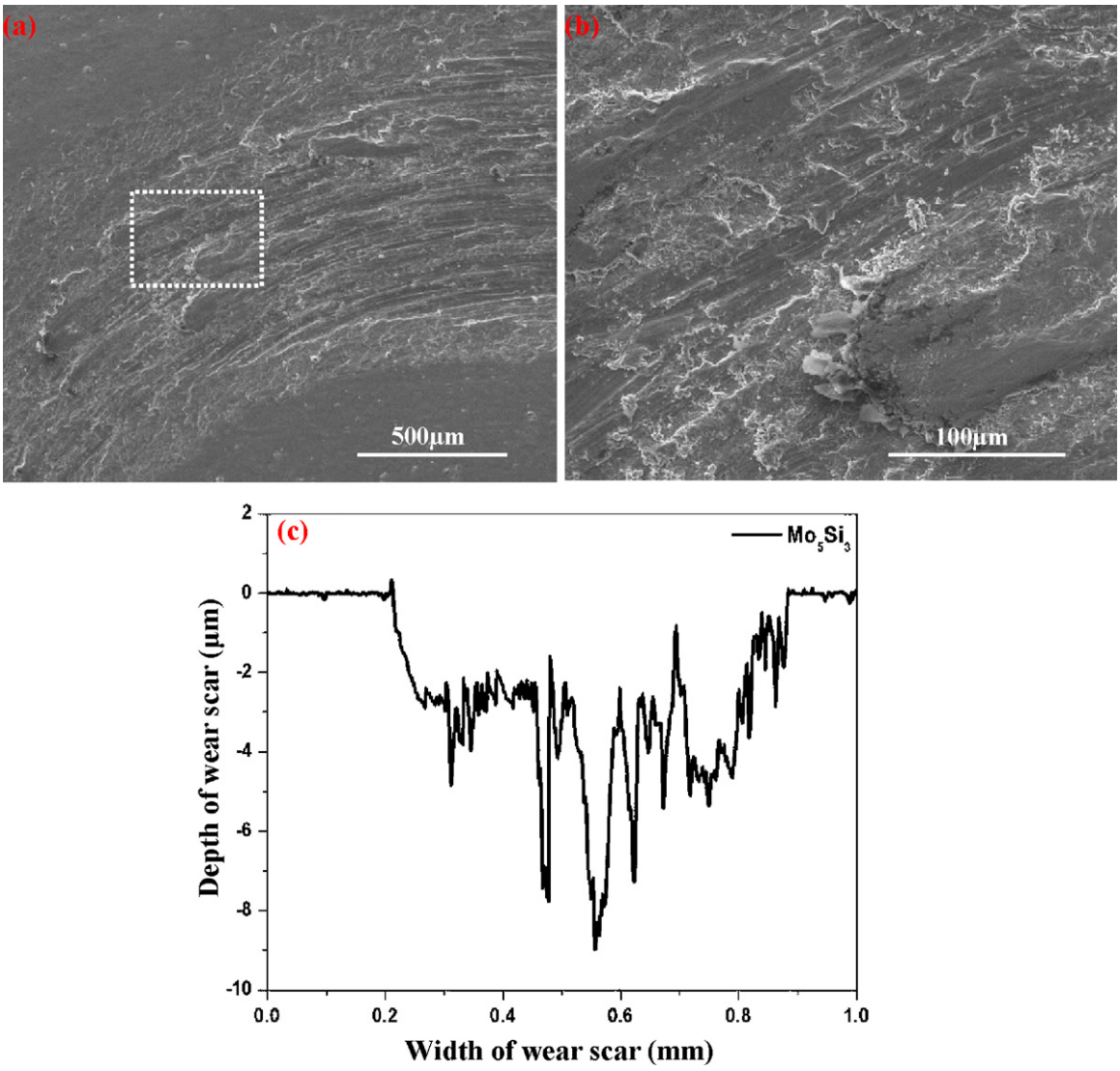

Fig. 10. The worn surface morphologies (a and b) and the cross-sectional profiles (c) of the nanocrystalline M_5Si_3 films at normal loads of 4.8 N under dry sliding conditions at 600 °C.

enriched in Ti and O by EDS analysis, confirming that it is probably titanium oxide detached from the worn surface of Ti6Al4V alloy, as shown in Fig. 9b. In addition, some traces of surface plastic deformation are also apparent on the wear debris, which is generated by brittle detachment of large particles from the surface and the subsequently squeezed between the friction pair. Thus, the surface of Ti6Al4V alloy suffers severe oxidative and abrasive wear at elevated temperature.

Fig. 10 shows the worn surface morphologies and cross-sectional profiles of the nanocrystalline Mo_5Si_3 films at the applied normal loads of 4.8 N under test temperature of 600 °C. As can be seen from Fig. 10a and higher magnificated area of Fig. 10a (Fig. 10b), the worn surface of nanocrystalline Mo_5Si_3 films has a rough morphology with evidence of severe delamination, plowing grooves that are located parallel to the sliding direction and some plastically deformed plateaus. As shown in Fig. 10(c), the maximum width and depth of wear scar are about 0.7 mm and 9 μm, respectively, and in some place depth of wear scar even reaches diffusion layer. Fig. 11 shows results of EDS analysis from outside wear scar and inside wear scar for the nanocrystalline Mo_5Si_3 films. EDS analysis of wear scar (see Fig. 11a) indicates the dominance of Ti (37.71 at.%), O (45.14 at.%), and a few of Zr (5.03 at.%), Mo (3.04 at.%), Al (5.33 at.%), Si (1.51 at.%) and V (2.25 at.%). In contrast, the unworn surface are highly enriched in O, Mo and Si elements with negligible amount of Ti, Al and V, as indicated in Fig. 11b. The XRD pattern of the worn surface of nanocrystalline Mo_5Si_3 film (see Fig. 12) shows the peaks of TiO_2 and MoO_3 along with the transferred counterpart ZrO_2, and no diffraction peaks due to crystalline SiO_2 could be observed, confirming its amorphous character. It is noteworthy that the high intensity of MoO_3 diffraction peaks mainly stems from the unworn surface rather than the worn surface, as a result of fairly less content of Mo inside the wear scar. Additionally, the presence of ZrO_2 on the worn surface suggests that the transfer from ZrO_2 ceramic ball to the counter surface occurs at contact areas during the high-temperature wear process. Such phenomenon correlates well with analysis results of wear debris. The wear debris consists of different size flake-like aggregates, and is enriched in O, Zr and Mo with minor amount Si, as indicated in Fig. 13. The result is a strong indication that ZrO_2 ball counterpart suffers likewise severe wear damage. However, in the case of the nanocrystalline Cr-alloyed Mo_5Si_3 films, SEM examinations reveal that the surface morphologies of the wear scars vary significantly with Cr content in the films, as evidenced by the fact that Cr content in the films should be a very important factor determining wear process (see Fig. 14). SEM morphology of worn surface for the nanocrystalline $(Mo_{0.78}Cr_{0.22})_5Si_3$

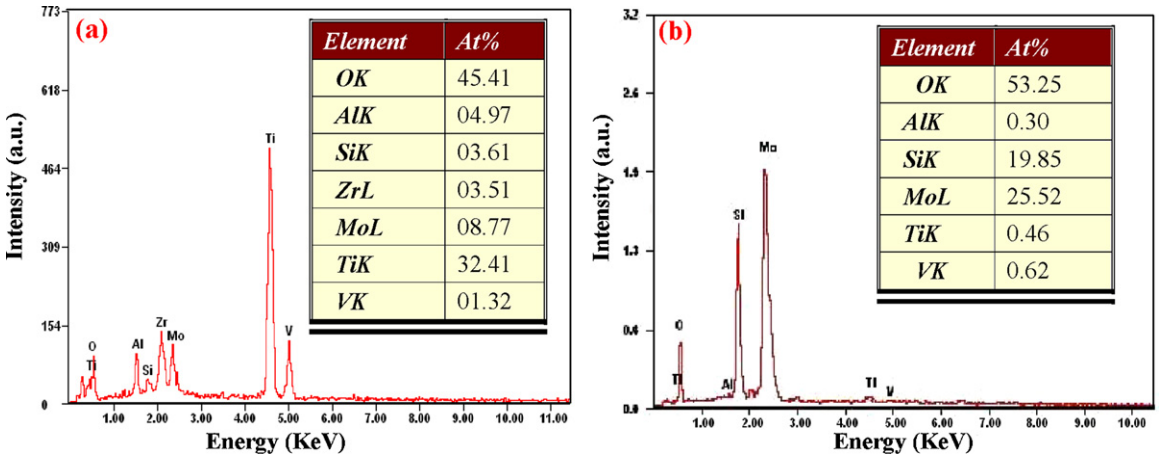

Fig. 11. EDS results of worn zone (a) and unworn zone (b) for the nanocrystalline M_5Si_3 films at normal loads of 4.8 N under dry sliding conditions at 600 °C.

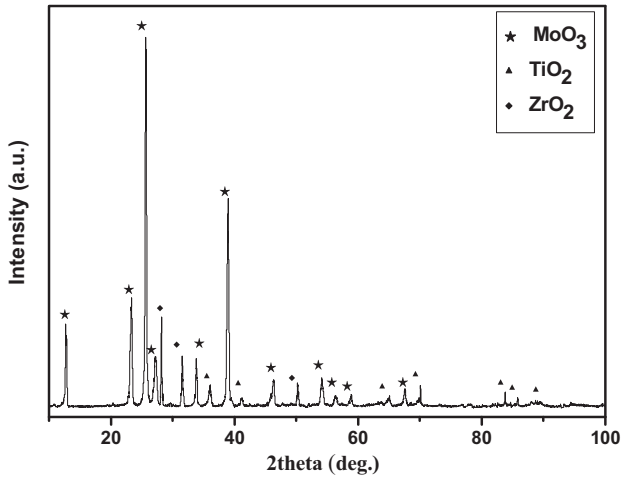

Fig. 12. The XRD pattern of the worn surfaces on the nanocrystalline Mo_5Si_3 film.

film shows some shallow craters of adhesive detachment with the surrounding fine wear debris, and is free from any scratches and plowing grooves characteristics, as shown in Fig. 14a. With further increasing the amount of Cr content, the wear tracks gradually become smoother, and are free of ploughing or delamination marks. Further, a pileup region, which is originated from compacting wear debris adhered to track surface, are visible at the boundary between the worn area and the unworn area, as indicated by white arrows in Fig. 14. An EDS analysis of the worn surface of nanocrystalline $(Mo_{0.57}Cr_{0.43})_5Si_3$ films has indicated the presence O, Mo, Cr, Si and Zr peaks in the EDS spectra, as shown in Fig. 15. It is important to note that the content of Zr is remarkably reduced, and similar finding is also confirmed by EDS analysis of wear debris (Fig. 16b). The size of wear debris from nanocrystalline $(Mo_{0.57}Cr_{0.43})_5Si_3$ film/ZrO_2 ball sliding pairs (Fig. 16a) at the applied normal loads of 4.8 N is much smaller than that obtained from nanocrystalline Mo_5Si_3 films/ZrO_2 ball sliding pairs under same test conditions, suggesting that couterpart ZrO_2 ceramic ball only undergoes mild wear. The cross-section profiles of the wear track (see Fig. 17) change significantly with increasing the amount of Cr content and wear depths of nanocrystalline Cr-alloyed Mo_5Si_3 films are dramatically decreased as compared to that of nanocrystalline Mo_5Si_3 films. Especially for nanocrystalline $(Mo_{0.57}Cr_{0.43})_5Si_3$ films, wear scar becomes extremely shallow and its depth is an order of magnitude smaller than that of nanocrystalline M_5Si_3 films. The XRD pattern obtained from the worn surface on the nanocrystalline $(Mo_{0.57}Cr_{0.43})_5Si_3$ films indicates (Fig. 18) that predominated oxides formed on the worn surface are MoO_3, $Cr_2(MoO_4)_3$ and ZrO_2.

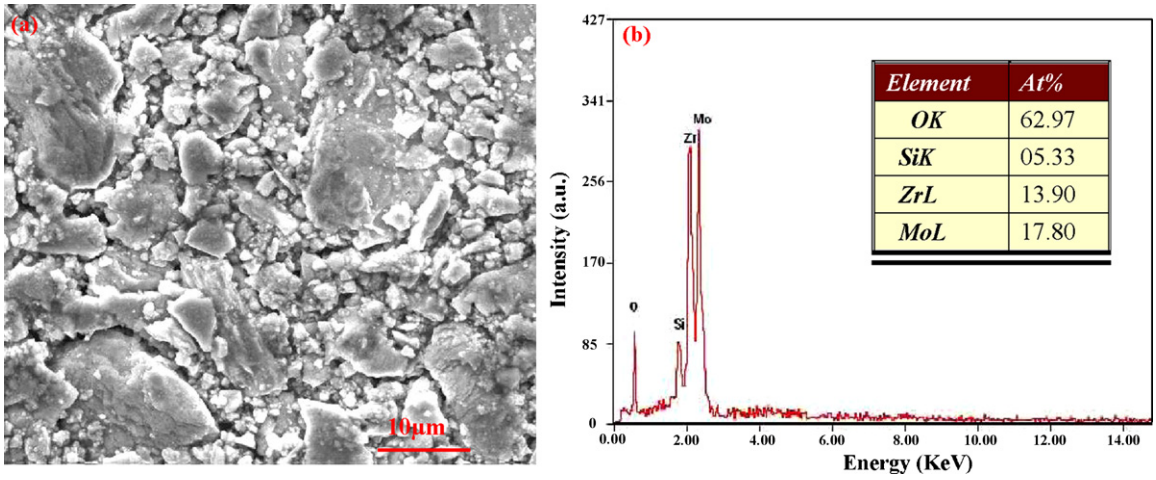

Fig. 13. Wear debris from nanocrystalline Mo_5Si_3 film/ZrO_2 ball sliding pairs: (a) wear debris morphology and (b) EDS analysis.

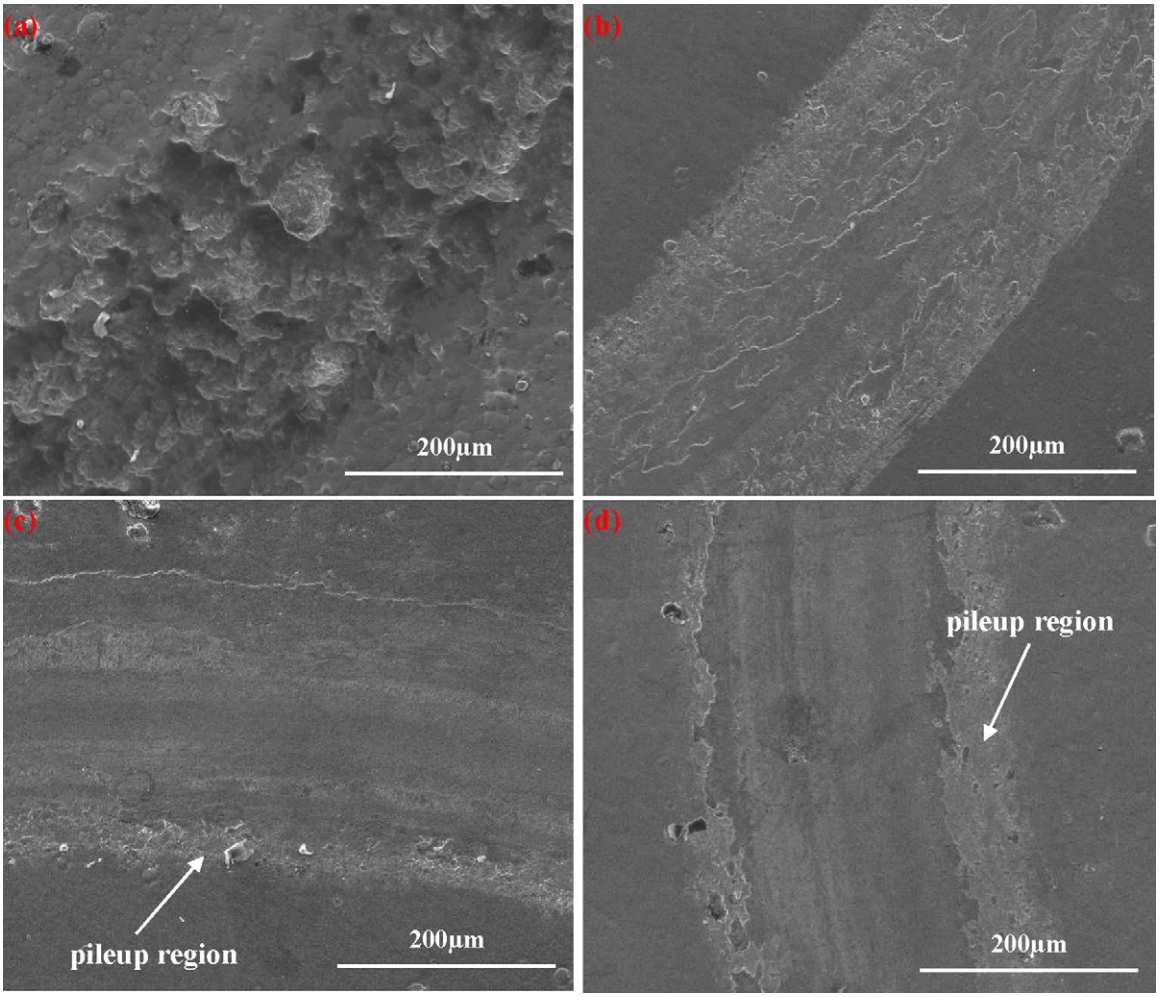

Fig. 14. The worn surface morphologies of the nanocrystalline Cr-alloyed Mo_5Si_3 films at normal loads of 4.8 N under dry sliding conditions at 600 °C. (a) $(Mo_{0.78}Cr_{0.22})_5Si_3$ film; (b) $(Mo_{0.75}Cr_{0.25})_5Si_3$ film; (c) $(Mo_{0.64}Cr_{0.36})_5Si_3$ film; (d) $(Mo_{0.57}Cr_{0.43})_5Si_3$ film.

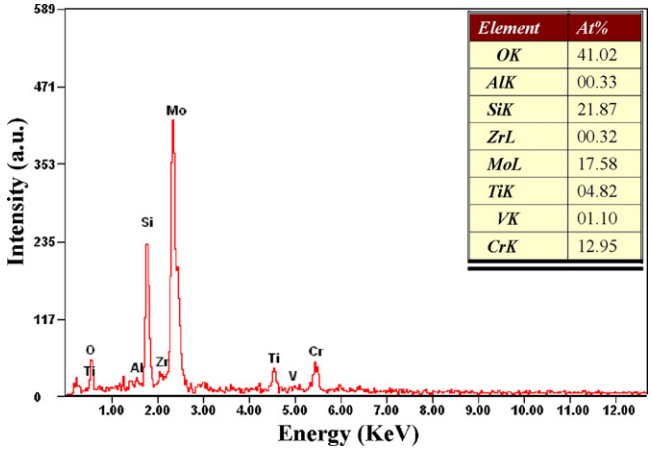

Fig. 15. EDS result of worn zone for the nanocrystalline $(Mo_{0.57}Cr_{0.43})_5Si_3$ film films at normal loads of 4.8 N under dry sliding conditions at 600 °C.

4. Discussion

As described above, it is reasonable to conclude that there is a close relationship between the content of Cr in the films and high temperature friction and wear properties of $(Mo_xCr_{1-x})_5Si_3$ films. Because of the high flash temperature induced by friction heat together with the elevated ambient temperature, the nanocrystalline $(Mo_xCr_{1-x})_5Si_3$ films are inevitably oxidized by a reaction between the films surface and the oxygen in air during high temperature wear process. Therefore, the surface oxidation products induced by tribochemical reaction are responsible for the noticeable difference in tribological properties of the nanocrystalline $(Mo_xCr_{1-x})_5Si_3$ films. In order to explore further the wear resistance provided by Cr alloying, the oxidation products and surface morphologies of the oxide scale formed on the nanocrystalline $(Mo_xCr_{1-x})_5Si_3$ films have been observed after isothermal oxidation experiments. Figs. 19 and 20 show macro-photograph and SEM micrographs of oxide scale formed on the five kinds of nanocrystalline $(Mo_xCr_{1-x})_5Si_3$ films specimen after isothermal oxidation in ambient air at 800 °C for different times, respectively. After isothermal oxidation at 800 °C for 2 min, plenty of white powder is widely distributed over the surface of nanocrystalline Mo_5Si_3 film, indicating that serious pest oxidation occurs (Fig. 19a). The oxidized surface is covered with white island-like clusters with loose and porous structure. By high magnification micrographs (inset in Fig. 20a), it reveals that those clusters consist of equiaxed crystal with Mo/O atomic ratio approaching 3, confirming that those clusters are MoO_3 (Fig. 20a). This is also identified by XRD analyses. The porous character of oxide scale appears on the surface of nanocrystalline Mo_5Si_3 film due to the volatilization of MoO_3 that has a sublimation temperature at 500 °C and above [29]. Thus the dominant oxidation reaction contributing to the formation of the

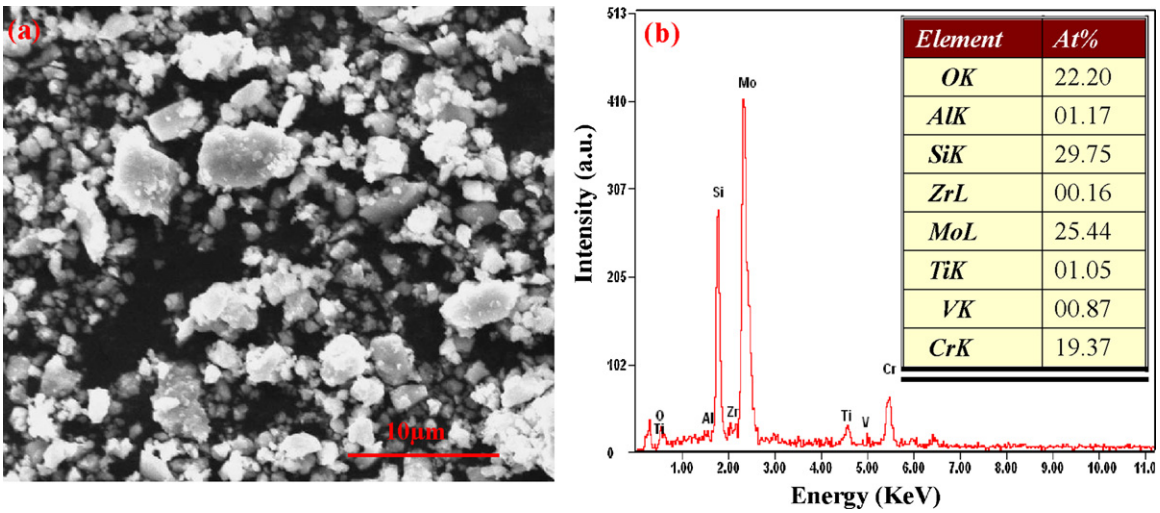

Fig. 16. Wear debris from nanocrystalline $(Mo_{0.57}Cr_{0.43})_5Si_3$ film/ZrO_2 ball sliding pairs: (a) wear debris morphology and (b) EDS analysis.

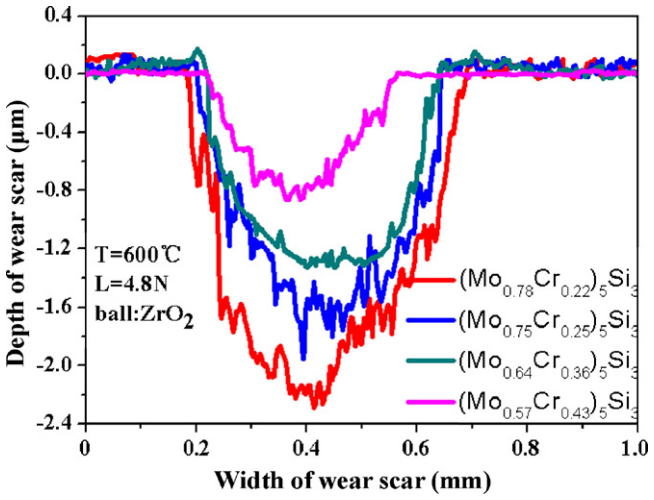

Fig. 17. The cross-sectional profiles of the nanocrystalline Cr-alloyed Mo_5Si_3 films at normal loads of 4.8 N under dry sliding conditions at 600 °C.

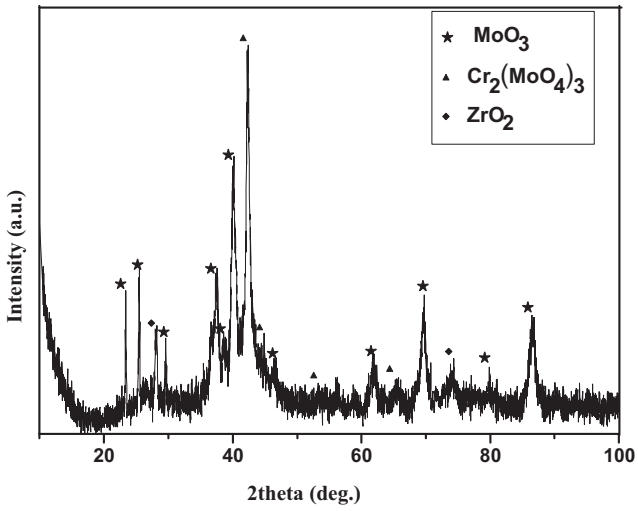

Fig. 18. The XRD pattern of the worn surfaces on the nanocrystalline $(Mo_{0.57}Cr_{0.43})_5Si_3$ film.

oxide scale constituents at 800 °C are:

$$2Mo_5Si_3 + 21O_2 \rightarrow 10MoO_3 \quad (\text{volatile}) + 6SiO_2 \qquad (1)$$

No pesting oxidation phenomenon is observed for the nanocrystalline Cr-alloyed Mo_5Si_3 films, as compared to the nanocrystalline Mo_5Si_3 film. In the case of nanocrystalline $(Mo_{0.78}Cr_{0.22})_5Si_3$ film, large area spalling of oxide scale has taken place after isothermal oxidation at 800 °C for 20 h (Figs. 19b and 20b). As a further increase in the amount of Cr content, the colour of the nanocrystalline $(Mo_xCr_{1-x})_5Si_3$(x = 0.75, 0.64, 0.57) films has been shifted from yellow to dark gray and then to silver gray, while simultaneously the surface of oxide scale becomes more dense and compact, as shown in Figs. 19c–e and 20c–e. This is indicative of the formation of a more protective oxide scale on the nanocrystalline $(Mo_xCr_{1-x})_5Si_3$ with higher Cr content. XRD results reveal that the oxide scales formed on nanocrystalline Cr-alloyed Mo_5Si_3 films consist of Cr_2O_3, $Cr_2(MoO_4)_3$ and amorphous SiO_2. This result is in agreement with that reported by StrÖm et al., who found that the oxide products formed on Cr-alloyed $MoSi_2$ after exposure at 450 °C in ambient air for 456 h are $Cr_2(MoO_4)_3$, MoO_3, and SiO_2 [30].

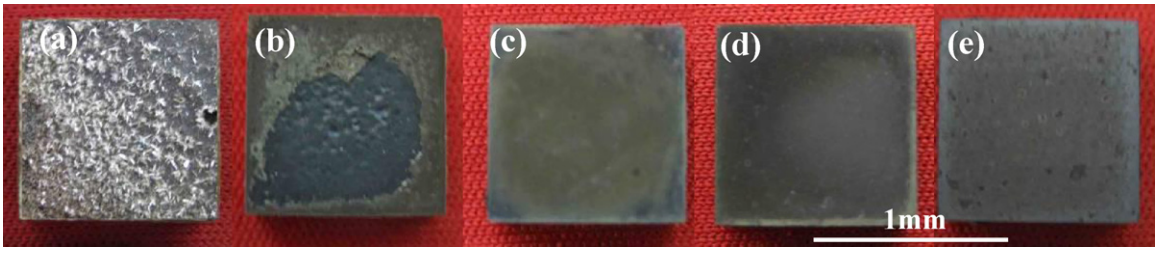

Fig. 19. Macro-photograph of the nanocrystalline $(Mo_xCr_{1-x})_5Si_3$ films specimen after isothermal oxidation in ambient air at 800 °C for different times: (a) Mo_5Si_3 film after oxidation of 2 min; (b) $(Mo_{0.78}Cr_{0.22})_5Si_3$ film; (c) $(Mo_{0.75}Cr_{0.25})_5Si_3$ film; (d) $(Mo_{0.64}Cr_{0.36})_5Si_3$ film and (e) $(Mo_{0.57}Cr_{0.43})_5Si_3$ film after oxidation of 20 h.

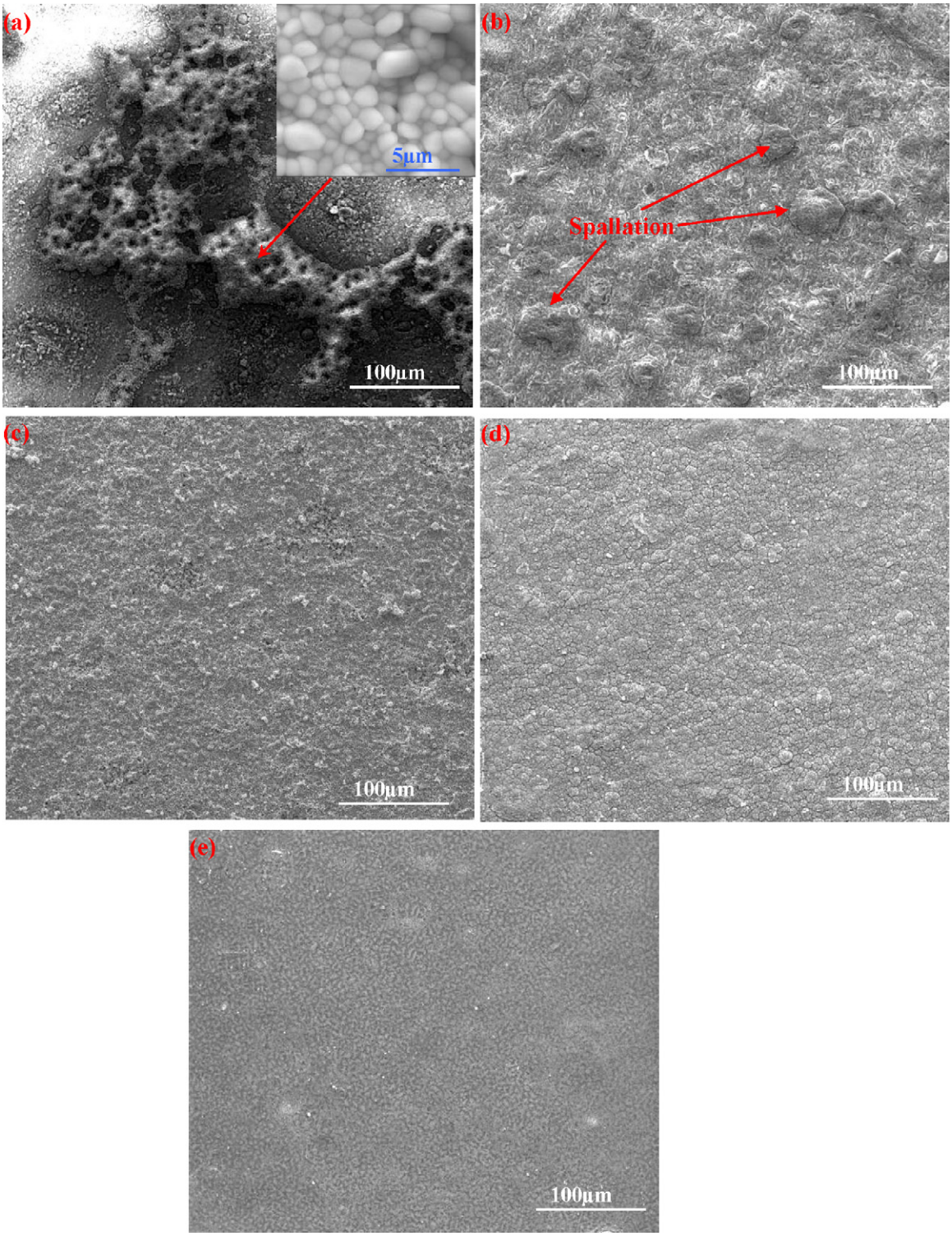

Fig. 20. SEM micrographs of oxide scale formed on the nanocrystalline $(Mo_xCr_{1-x})_5Si_3$ films specimen after static thermal oxidation in ambient air at 800 °C for different times: (a) Mo_5Si_3 film after oxidation of 2 min; (b) $(Mo_{0.78}Cr_{0.22})_5Si_3$ film; (c) $(Mo_{0.75}Cr_{0.25})_5Si_3$ film; (d) $(Mo_{0.64}Cr_{0.36})_5Si_3$ film and (e) $(Mo_{0.57}Cr_{0.43})_5Si_3$ film after oxidation of 20 h.

Thus, the nanocrystalline Cr-alloyed Mo_5Si_3 films are expected to oxidize through the reaction:

$$12(Mo_xCr_{1-x})_5Si_3(x = 0.78,\ 0.75,\ 0.64,\ 0.57) + (45x+81)O_2 \rightarrow 20xCr_2(MoO_4)_3 + 36SiO_2 + 10(3-5x)Cr_2O_3 \quad (2)$$

On the basis of isothermal oxidation experiments, it can be concluded that oxidation resistance of the nanocrystalline $(Mo_xCr_{1-x})_5Si_3$ shows an increase with Cr additions, and the oxide scale on its surface can play a role of barrier between the films and ambient air by suppression the diffusion of oxygen.

Owing to its very fine size and high surface area, the nanocrystalline Mo_5Si_3 film is liable to react with the oxygen at the

contact surface when sliding against ZrO_2 balls. As a result, the performances of an oxide film formed by tribo-oxidation, including mechanical properties of the oxide film and bond strength between the oxide film and the underlying nanocrystalline Mo_5Si_3 film, determine the wear resistance of the nanocrystalline $(Mo_xCr_{1-x})_5Si_3$ film. According to the XRD diffraction patterns corresponding to worn surface, surface of the nanocrystalline Mo_5Si_3 film has been oxidized to form the MoO_3 crystal and amorphous SiO_2. MoO3 with an orthorhombic structure is known as a solid lubricant, and has a lower friction coefficient at elevated temperature, due to the fact that it possesses a homologous series with planar faults in the crystal structure, leading to a low shear strength along (0 1 0) planes [31,17,32]. However, MoO_3, as a volatile oxide, prone to evaporate from the worn surface, leaving behind a porous tribo-oxidation film surface, where accelerates oxidation by facilitating the fast oxygen transport to the oxide/Mo silicide interface. Simultaneously, the effect of tribo-oxidation produces high internal stresses within oxide film, stemming from remarkable volume expansion as a consequence of different densities of the oxidation product and Mo_5Si_3 film. A loose and poorly protective tribo-oxidation film is easily removed by spalling or plowing of hard asperities on the ZrO_2 ball, and thereafter reoxidation of the exposed interior Mo_5Si_3 film occurs. Hence, the nanocrystalline Mo_5Si_3 film is susceptible to oxidative wear caused by repetitive disruption of oxide films. Besides, owing to the volatilization of MoO_3, the amount of residual self-lubricating MoO_3 on the wear track surface is constantly reduced, resulting in the relatively high friction coefficient.

As referred to above, oxidation behaviour of the nanocrystalline Cr-alloyed Mo_5Si_3 films is significantly improved compared with the nanocrystalline Mo_5Si_3 film, and the oxidation resistance of the nanocrystalline Cr-alloyed Mo_5Si_3 films is directly proportional to the amount of Cr addition by morphologies observation of oxide scale. This comes from the fact that the additions of Cr to Mo_5Si_3 film play an important role in obstructing or trapping the evaporation of MoO_3 by the formation of protective composite oxide scales. A denser tribo-oxidation oxide film has more excellent mechanical properties, and can provide better protection the surface against combine attack by mechanical wear action and oxidation. During wear process, the underlying the nanocrystalline Cr-alloyed Mo_5Si_3 films acts as a reservoir to continuously supply Mo to form the lubricious MoO_3. Therefore, with increasing Cr content in $(Mo_xCr_{1-x})_5Si_3$ films, the changing trend of oxidation resistance is in harmony with that of wear resistance. As the wear process continued, the oxide film developed on the surfaces may be partially removed by the action of the counterpart, accompanying by the formation of oxide wear debris. As shown in Fig. 16a, the size of the delaminated wear debris from Cr-alloyed Mo_5Si_3 films/ZrO_2 ball sliding pairs is much smaller than that obtained from Mo_5Si_3 film/ZrO_2 ball sliding pairs. One difference from the large wear debris particles is that smaller wear debris is apt to be entrapped in the contact interface of frictional pairs. In the early stage of high-temperature sliding wear, a small amount of fine wear debris is predominantly embedded in grooves of worn surface or act as a lubricious medium. As wear time increases, the amount of wear debris is gradually increased. A fraction of wear debris is driven away from the contact surface, which products the pileup region formed the outside of the wear track, while others is retained between the contacting surfaces [33,34]. Those adhered wear debris may be agglomerated and compacted, followed by plastic smearing to produce a continuous, smooth and protective surface layer, thus mitigating friction and wear. In addition, high hardness of the nanocrystalline Cr-alloyed Mo_5Si_3 films provides enough supporting for the soft tribo-oxidation surface layer, and this negative hardness-gradient is a desirable surface characteristic to achieve a low wear rate [31].

5. Conclusions

In summary, in order to improve tribological properties of titanium alloys, five kinds of sputter-deposited nanocrystalline $(Mo_xCr_{1-x})_5Si_3$(x = 1, 0.78, 0.75, 0.64, 0.57) films with the average grain size of 8 nm have been successfully prepared on Ti6Al4V alloy substrates by double cathode glow discharge. Compared with the Ti6Al4V alloy, at the same applied normal load, the coefficient of friction values of the nanocrystalline $(Mo_xCr_{1-x})_5Si_3$ films are reduced by 0.2–0.3, and specific wear rates decrease by two orders of magnitude and are around or lower than 10^{-6} mm^3/(N m). For the nanocrystalline $(Mo_xCr_{1-x})_5Si_3$ films, the specific wear rate decreases with increasing Cr content in the films at the same applied load. Results show that there is a close relationship between oxidation behaviour and wear resistance of the nanocrystalline $(Mo_xCr_{1-x})_5Si_3$ films. With increasing Cr content in $(Mo_xCr_{1-x})_5Si_3$ films, the changing trend of oxidation resistance is in harmony with that of wear resistance.

Acknowledgements

The authors gratefully acknowledge the financial support of the Aeronautics Science Foundation of China under project No. 2009ZE52047 and Key Program of Jiangsu province Natural Science foundation of China under project No. BK2010073.

References

[1] F. Wang, Q.L. Bi, X.B. Wang, W.M. Liu, Tribol. Int. 41 (2008) 158–165.
[2] A. Tóth, M. Mohai, T. Ujvári, T. Bell, H. Dong, I. Bertóti, Surf. Coat. Technol. 186 (2004) 248–254.
[3] C.H. HagerJr, J.H. Sandersb, S. Sharma, Wear 265 (2008) 439–451.
[4] D.S. Ming, Y.Z. Wei, Wear 263 (2007) 653–657.
[5] A. Molinari, G. Straffelini, B. Tesi, T. Bacci, Wear 208 (1997) 105–112.
[6] H. Dong, T. Bell, Wear 238 (2000) 131–137.
[7] Y. Wang, H.M. Wang, Appl. Surf. Sci. 229 (2004) 81–86.
[8] M.M. Silva, M. Ueda, L. Pichon, H. Reuther, C.M. Lepienski, Nucl. Instrum. Methods B 257 (2007) 722–726.
[9] K.T. Rie, T. Stucky, R.A. Silva, E. Leitão, K. Bordji, J.-Y. Jouzeau, D. Mainard, Surf. Coat. Technol. 74–75 (1995) 973–980.
[10] D.H. Kuo, K. Huang, Surf. Coat. Technol. 135 (2001) 150–157.
[11] B. Skoric, D. Kakas, N. Bibic, M. Rakita, Surf. Sci. 566 (2004) 40–44.
[12] T. Polcar, R. Novák, P. Široký, Wear 260 (2006) 40–49.
[13] C.L. Yeh, W.H. Chen, J. Alloys Compd. 439 (2007) 59–66.
[14] C.L. Yeh, H.J. Wang, Intermetallics 15 (2007) 1277–1284.
[15] Z. Chen, Y.W. Yan, J. Alloys Compd. 413 (2006) 73–76.
[16] F. Chu, D.J. Thoma, K.J. McClellan, P. Peralta, Mater. Sci. Eng. A 261 (1999) 44–52.
[17] T. Iizuka, H. Kita, Wear 258 (2005) 877–889.
[18] F. Chu, D.J. Thoma, K. McClellan, P. Peralta, Y. He, Intermetallics 7 (1999) 611–620.
[19] K. Yoshimi, M.H. Yoo, A.A. Wereszczak, S.M. Borowicz, E.P. George, E. Miura, S. Hanada, Mater. Sci. Eng. A 329–331 (2002) 228–234.
[20] A. Mufit, K.M. Mitchell, J.K. Matthew, J.T. Andrew, J.H. Jesse, C. Bruce, Mater. Sci. Eng. A 261 (1999) 16–23.
[21] J. Xu, Z. Xu, X.S. Xie, Z. Xu, W.J. Liu, Vacuum 72 (2004) 489–500.
[22] J. Xu, J. Sun, S.Y. Jiang, Mater. Lett. 63 (2009) 1082–1084.
[23] W.C. Oliver, G.M. Pharr, J. Mater. Res. 7 (1992) 1564–1583.
[24] E. StrÖm, J. Zhang, S. Eriksson, C.H. Li, D. Feng, Mater. Sci. Eng. A 329–331 (2002) 289–294.
[25] A.R. Cox, R. Brown, J. Less-Common Met. 6 (1964) 51–69.
[26] X.M. Peng, C.Q. Xia, Y.Y. Liu, J.H. Wang, Surf. Coat. Technol. 203 (2009) 3306–3311.
[27] A. Misra, J.J. Petrovic, T.E. Mitchell, Scripta Mater. 40 (1999) 191–196.
[28] P. Perez, Surf. Coat. Technol. 191 (2005) 293–302.
[29] N. Floquet, O. Bertrand, J.J. Heizmann, Oxid. Met. 37 (1992) 253–280.
[30] E. StrÖm, Y. Cao, Y.M. Yao, Trans. Nonferr. Met. Soc. 17 (2007) 1282–1286.
[31] Q. Yang, L.R. Zhao, P.C. Patnaik, X.T. Zeng, Wear 261 (2006) 119–125.
[32] I.W. Lyo, H.S. Ahn, D.S. Lim, Surf. Coat. Technol. 163–164 (2003) 413–421.
[33] F.H. Stott, M.P. Jordan, Wear 250 (2001) 391–400.
[34] F.H. Stott, Tribol. Int. 35 (2002) 489–495.